HHS Public Access

Author manuscript

Nature. Author manuscript; available in PMC 2020 January 07.

Published in final edited form as:

Nature. 2018 August ; 560(7716): 97–101. doi:10.1038/s41586-018-0354-1.

Differential tuning of excitation and inhibition shapes direction selectivity in ferret V1

Daniel E. Wilson[1,2,3,4,*], **Benjamin Scholl**[1,*], **David Fitzpatrick**[1]

[1]Max Planck Florida Institute for Neuroscience, Jupiter, Florida 33458, USA

[2]IMPRS for Brain and Behavior, Florida Atlantic University, Jupiter, Florida 33458, USA

[3]Integrative Biology and Neuroscience Graduate Program, Florida Atlantic University, Jupiter, Florida 33458, USA

[4]Present address: Department of Neurobiology, Harvard Medical School, Boston, Massachusetts 02115, USA

Abstract

To encode specific sensory inputs, cortical neurons must generate selective responses for distinct stimulus features. In principle, a variety of factors contribute to a cortical neuron's response selectivity: the tuning and strength of excitatory[1–3] and inhibitory synaptic inputs[4–6], dendritic nonlinearities[7–9], and spike threshold[10,11]. Here we employ a combination of techniques including *in vivo* whole-cell recording, synaptic and cellular resolution *in vivo* two photon calcium imaging, and GABAergic-selective optogenetic manipulation to dissect the factors contributing to direction selective responses of layer 2/3 neurons in ferret visual cortex (V1). Two-photon calcium imaging of dendritic spines[12,13] revealed that each neuron receives a mixture of excitatory synaptic inputs selective for the somatic preferred or null direction of motion. The relative number of preferred- and null-tuned excitatory inputs predicted a neuron's somatic direction preference, but failed to account for the degree of direction selectivity. In contrast, *in vivo* whole-cell patch clamp recordings revealed a striking degree of direction selectivity in subthreshold responses that was significantly correlated with spiking direction selectivity. Subthreshold direction selectivity was predicted by the magnitude and variance of the response to the null direction of motion, and several lines of evidence including conductance measurements demonstrate that differential tuning of excitation and inhibition suppresses responses to the null direction of motion. Consistent with this idea, optogenetic inactivation of GABAergic neurons in layer 2/3 reduced direction selectivity by enhancing responses to the null direction. Furthermore, using a new technique to optogenetically map connections of inhibitory neurons in layer 2/3 *in vivo*, we find that layer 2/3

Correspondence: David Fitzpatrick, Max Planck Florida Institute for Neuroscience, 1 Max Planck Way, Jupiter, FL 33458, David.fitzpatrick@mpfi.org.

*These authors contributed equally to this work

Author contributions

D.E.W., B.S., and D.F. conceived experiments. D.E.W. and B.S. performed experiments and analyzed data with guidance from D.F. D.E.W., B.S., and D.F. wrote the paper.

Competing financial interests

The authors declare no competing financial interests.

inhibitory neurons make long-range, intercolumnar projections to excitatory neurons that prefer the opposite direction of motion. We conclude that intracortical inhibition exerts a major influence on the degree of direction selectivity in layer 2/3 of ferret V1 by suppressing responses to the null direction of motion.

Using sparse expression of GCaMP6s and two-photon calcium imaging[12,13], we first determined a neuron's somatic preferred direction using drifting grating stimuli (example cell, Fig. 1a) and then presented the somatic preferred and null directions while imaging spines on apical and basal dendrites. Individual dendritic branches contained spines that responded preferentially to either the somatic preferred or null directions (example branch, Fig. 1b); this diversity existed throughout the dendritic field of single neurons (Fig. 1c). By quantifying spine responses using a direction selectivity index (DSI, see methods) we found that spines tuned for the somatic preferred and null directions exhibited somewhat different DSI values (Fig. 1d, Wilcoxon rank-sum, $P = .002$, $n = 384$ preferred spines, $n = 233$ null spines from $n = 17$ cells from 10 animals), and in 8/12 direction-selective cells (soma DSI>0.3), we observed more spines tuned to the somatic preferred direction than to the null (Fig. 1e). Similar fractions of spines from basal (300/498) and apical (84/119) dendrites responded more strongly to the somatic preferred direction (60.2% and 70.6%, respectively). We then computed bootstrapped sums of normalized spine responses (see Methods) to assess the relation between the DSI of a neuron's inputs and soma. Summed excitatory synaptic input was weakly tuned (summed spine DSI .1 ± .1, median ± IQR, $n = 17$ cells) and we found no correlation between summed spine and somatic DSI across our sample (Fig. 1f, $r = -.08$, $P = .75$, $n = 17$ cells), regardless of how we assessed synaptic input direction selectivity (see Methods, Extended Data Fig. 1a-b). Taken together, these data emphasize that functional specificity of excitatory synaptic inputs converging onto individual layer 2/3 neurons is sufficient to account for somatic direction preference, but fails to explain the degree of somatic direction selectivity.

Previous work suggests that spike threshold amplifies weak biases in excitatory synaptic inputs to enhance spiking direction selectivity of neurons in layer 4 of cat V1[14]. To examine whether subthreshold membrane potential (V_m) responses reflect the weak biases in excitatory inputs demonstrated by our spine imaging, we made whole-cell patch clamp recordings from layer 2/3 neurons using a K^+-based internal solution ($n = 76$ cells from 23 animals, example, Fig. 2a-b). A majority of cells (78%, $n = 54/69$) showed strong spiking direction selectivity (Extended Data Fig. 2). Surprisingly, nearly half of the cells with direction-selective spiking responses (48%, $n = 26/54$) showed strong direction tuning in their V_m (Fig. 2c), and the degree of V_m selectivity was correlated with spiking selectivity ($n = 69$ cells, $r = .56$, $P = 5.67e\text{-}7$). The strong direction selectivity evident in V_m responses is in sharp contrast to the weak selectivity predicted by the distribution of excitatory synaptic inputs and forced us to consider factors that might contribute to the strong direction tuning of V_m responses. In principle, the emergence of strong subthreshold tuning from broadly tuned excitatory inputs could reflect mechanisms that enhance the effectiveness of excitatory inputs tuned to the preferred direction, diminish the effectiveness of excitatory inputs tuned to the null direction, or some combination of these factors. To distinguish among these alternatives, we asked if there was a consistent relationship between subthreshold selectivity

and subthreshold response amplitude to preferred and null direction stimuli. We found no correlation between V_m DSI and subthreshold response amplitude to the preferred direction (Fig. 2d, $r = -.001$, $P = .99$, $n = 76$). In contrast, we found a strong anticorrelation between V_m DSI and null direction response amplitude (Fig. 2e, $r = -.69$, $P = 5.07e\text{-}12$, $n = 76$). These results point to factors impacting null direction responses as being important in determining V_m selectivity.

We then considered the degree to which inhibitory inputs contribute to subthreshold responses to the null direction of motion[5,15,16]. Theoretical models predict that when levels of inhibition are high relative to excitation, not only is there a reduction in the level of depolarization, but also a reduction in the 'noise' or V_m variability[17,18]. We therefore examined the relationship between subthreshold DSI and V_m noise (see Methods) for the preferred direction and observed no significant correlation (Fig. 2f, $r = -.10$, $P = .39$, $n = 76$ cells). Instead, we uncovered a strong anticorrelation between subthreshold DSI and V_m noise at the null direction (example, Extended Data Fig. 3; Fig. 2g, $r = -.61$, $P = 6.94e\text{-}9$, $n = 76$ cells), consistent with a significant role for inhibition to the null direction in shaping subthreshold direction selectivity of layer 2/3 neurons.

The idea that inhibition contributes to direction selectivity stands in contrast to a number of studies showing that inhibition functions to normalize cortical activity[19,20]. These studies show that excitation and inhibition are generally co-tuned[4,14,20,21] while our observations suggest that the tuning of excitatory and inhibitory inputs onto direction-selective neurons are dissimilar. To directly measure excitatory (G_e) and inhibitory (G_i) synaptic conductances underlying direction selectivity, we performed whole-cell patch-clamp recordings using a Cs^+-based internal solution[14] and recorded V_m responses to drifting gratings at different current steps to extract synaptic conductances and their direction tuning (example, Fig. 3a-b, see Methods). We observed a wide range of direction selectivity present in synaptic conductances and found that excitatory and inhibitory DSI were not correlated (Fig. 3c, $r = .043$, $P = .91$, $n = 10$ cells from 7 animals) and therefore not co-tuned. In half of our recorded neurons, excitation and inhibition preferred opposite directions ($\Delta\theta > 135^o$) and across the population there was a significant bias toward preferring opposite directions (Extended Fig. 4a). Despite a lack of co-tuning, excitation and inhibition shared similar tuning bandwidth (Extended Data Fig. 4b).

Understanding the impact of inhibitory conductances on subthreshold responses requires considering co-occurring excitatory conductances. Thus, we measured the relative strength of inhibition as the ratio of inhibitory to excitatory conductance (G_i/G_e) and found that G_i/G_e was systematically larger for null direction than for preferred direction stimuli (Fig. 3e, WSR, $P = .037$, $n = 10$). Moreover, the direction selectivity of predicted V_m from empirically measured synaptic conductances (population tuning curves in Extended Data Fig. 4c)[22] was significantly correlated with the G_i/G_e ratio at the null direction (Fig. 3f, $r = .81$, $P = .008$, $n = 10$ cells from 7 animals) but not the preferred direction (Extended Data Fig. 5). Consistent with our spine imaging data (Fig. 1f), predicted V_m direction selectivity was not correlated with the direction tuning of excitation alone (Fig. 3d, $r = .49$, $P = .15$, $n = 10$). Our measurements of synaptic conductances suggest that relatively stronger inhibitory input at the null direction acts to enhance somatic direction selectivity.

If relatively greater G_i/G_e at the null direction contributes to direction selectivity in layer 2/3, inactivating GABAergic neurons in layer 2/3 would reduce suppression at the null-direction and reduce selectivity, as suggested by previous pharmacological studies[23]. To test this hypothesis, we optogenetically suppressed layer 2/3 GABAergic neurons by expressing GtACR2 under control of the mDlx enhancer and measured direction selectivity using whole-cell patch clamp recordings with K^+-based internal solution. Optogenetic inactivation of GABAergic neurons (example, Extended Data Fig. 6) increased evoked response amplitude (example, Fig. 3g) and reduced V_m DSI (Fig. 3h, $P = .004$, WSR, $n = 16$ cells from 4 animals) and spiking DSI (Extended Data Fig. 7a). Importantly, changes in subthreshold direction selectivity were not related to the absolute V_m depolarization induced by GABAergic photoinhibition in individual neurons (Extended Data Fig. 7b). Instead, the degree to which null-direction responses were modulated by GABAergic suppression (see Methods) depended on the cell's V_m DSI (Fig. 3j, $r = .56$, $P = .025$, $n = 16$ cells), while no such relationship was observed for modulation of preferred-direction responses (Fig. 3i, $r = .20$, $P = .46$, $n = 16$ cells). Based on these results, inhibition enhances subthreshold direction selectivity through null-direction suppression and we would predict that GABAergic neurons preferring the opposite direction would contribute to this suppression.

GABAergic neurons in ferret V1 are direction-tuned and form direction columns[24] aligned with the underlying intrinsic signal direction preference map (Extended Data Fig. 8a-b). For GABAergic neurons to innervate oppositely tuned excitatory cells, their projections must extend beyond the local direction domain and into adjacent cortical columns. This would be inconsistent with studies from mouse V1 where excitatory neurons receive inhibitory input from local (within 100–200 μm) GABAergic neurons[25–27]. However, in carnivore V1, it has been shown that GABAergic neurons make axonal projections spanning longer distances[28,29]. To test whether GABAergic neurons project beyond their local cortical column, we labeled axon projections with punctate injections of AAV2/1.mDlx.GCaMP6s and characterized the direction tuning of axon projections at sites distal to the injection location (example, Fig. 4a-d). A substantial fraction (60.5%) of long-range projecting individual boutons exhibited direction-selective responses (example, Fig. 4e, population median .39 ±.46 IQR, n = 815 boutons, 8 fields of view from 2 animals) and diverse direction preferences when compared to the intrinsic signal map (example, Fig. 4d). We found a surprising abundance of direction-selective GABAergic boutons tuned to the opposite direction of direction domains (Fig. 4f). Further, individual bouton preferences were significantly different from the map (Monte Carlo significance test, $P < .001$, $n = 493$ boutons), providing an anatomical substrate for synaptic inhibition observed in our previous measurements.

To examine whether individual neurons receive inhibitory synaptic input from distant GABAergic neurons, we developed a technique called Somatically Targeted Optogenetic Membrane Potential Mapping (STOMPM) to directly map the spatial connectivity of inhibitory onto excitatory neurons *in vivo*. We localized Channelrhodopsin-2 to the soma and proximal dendrites of GABAergic neurons using a Kv2.1 targeting motif (Fig. 4g) to prevent stimulation of neuropil and enhance our functional resolution. As GABAergic neuron direction preferences are smoothly mapped in a columnar fashion[24] (Extended Data Fig. 8), we used patterned photostimulation driven by a DLP projector[30] to activate

GABAergic neurons in local cortical regions (~100–200 μm, Fig. 4g) while recording from single neurons to measure inhibitory postsynaptic potentials (IPSPs) (example cell, Extended Data Fig. 9). Optical stimulation evoked robust IPSPs (examples, Fig 4h) even at spots distant from recorded cells. Neurons received inhibitory synaptic input from long distances (example, Fig. 4i); inhibitory input fields often exceeded 1mm along their major axis (example, Fig. 4i-j, summary data in Fig. 4k, major axis length 930 ± 278μm, median ± IQR, n = 21 cells from 7 animals) and many inputs arrived from distances greater than 500 μm (Extended Data Fig. 10), and we recognize that these measures likely underestimate the total extent of input field size (see Methods). Finally, we aligned our stimulation grid with the intrinsic signal direction preference map (Fig. 4l) to characterize the functional origin of evoked IPSPs. Indeed, we found that neurons with direction-selective V_m (n =7 cells, mean tuning curve in Fig. 4m) received almost equivalent inhibitory synaptic input from null-tuned direction domains as preferred-tuned (Fig. 4n).

Previous studies suggest inhibition and excitation are generally co-tuned[4,14,20,21,31] (Fig. 4o) as shown for orientation selectivity in mouse V1[4] and layer 4 simple cells of cat V1[11], albeit with distinct temporal dynamics[4], acting to scale or gate overall responses[22]. In contrast, we find that cortical inhibition can suppress responses to specific stimuli through differential tuning with excitation (Fig. 4o). Such differential tuning can arise through multiple combinations of excitation and inhibition, such that null-direction suppression is driven by either null-biased or equivalent inhibitory inputs for both directions (Fig. 4o). Differential tuning can enhance subthreshold selectivity, which is further augmented through spike threshold[11] (Fig. 4o). Our findings are conceptually similar to those in retinal ganglion cells[32], but differ in exact circuit implementation as ganglion cell direction selectivity arises through inhibitory input mediated by starburst amacrine cells. One factor we did not consider is the temporal interplay between excitation and inhibition, which could play an important contributing role in enhancing selectivity[31]. Taken together with previous studies, the selective responses of cortical neurons are built with a broadly tuned palette of excitatory synaptic inputs that is further refined by enhancing responses to the preferred stimulus[7,8,12] and suppressing responses to non-preferred stimuli.

Methods

All procedures were performed according to NIH guidelines and approved by the Institutional Animal Care and Use Committee at Max Planck Florida Institute for Neuroscience.

Constructs

pAAV-mDlx-GCaMP6f-Fishell-2[33] was a gift from Gordon Fishell (Addgene plasmid # 83899). pFUGW-hGtACR2-EYFP[34] was a gift from John Spudich (Addgene plasmid # 67877). pCAG-CyRFP1 was a gift from Ryohei Yasuda (Addgene plasmid # 84356). pAAV.mDlx.ChR2-FLAG-Kv2.1.p2a.H2b-CyRFP was a gift from McLean Bolton.

Virus injection

Female ferrets aged ~P30 (Marshall Farms) were anesthetized with ketamine (50 mg/kg) and isoflurane (1–3%, delivered in O_2), then intubated and artificially respirated. Atropine was administered to reduce secretions and a 1:1 mixture of lidocaine and bupivacaine administered subcutaneously in the scalp. Animals were placed on a feedback-controlled heating pad to maintain internal temperature at 37°C. Under sterile surgical conditions, a small craniotomy (0.8 mm diameter) was made over the visual cortex 7–8mm lateral and 2–3mm anterior to lambda.

For spine imaging, we injected (52 nl per depth) a mixture (1:100000) of AAV1.hSyn.Cre and AAV1.Syn.GCaMP6s (UPenn, ~1e13 GC/mL) at 400 and 200 μm below the pia through beveled glass micropipettes (10–15 μm outer diameter). For imaging GABAergic axons or somata, we injected 5–30 nl of AAV1.mDlx.GCaMP6s at 400 and 200 μm below the pia. For optogenetic inactivation experiments, we injected 1 μl of AAV1.mDlx.GtACR2-eYFP (titer >1e13 GC/mL, custom preparation from Vigene) at 400 and 200 μm below the pia through beveled glass micropipettes (15–20 μm outer diameter). For STOMPM (see below), we injected 1 μl of AAV1.mDlx.ChR2-FLAG-Kv2.1.p2a.H2b-CyRFP (titer> 1e13 GC/mL, custom preparation from Vigene) through beveled glass micropipettes (15–20 μm outer diameter). To prevent dural regrowth and adhesion, the craniotomy was filled with sterile 1% w/v agarose (Type IIIa, Sigma-Aldrich).

Cranial window

After 3–5 weeks of expression, ferrets were anesthetized with 50mg/kg ketamine and 1–3% isoflurane. Atropine and bupivacaine were administered as in virus injection procedure. Animals were placed on a feedback-controlled heating pad to maintain an internal temperature of 37 to 38 °C. A tracheotomy was performed and an endotracheal tube installed to artificially respirate the animal. Isoflurane was delivered between 1 and 3% throughout the surgical procedure to maintain a surgical plane of anesthesia. An intravenous cannula was placed to deliver fluids. ECG, end tidal CO2, external temperature, and internal temperature were continuously monitored throughout the imaging session.

The scalp was retracted and a custom titanium headplate adhered to the skull using C&B Metabond (Parkell). A 6 to 7 mm craniotomy was performed at the viral injection site and the dura retracted to reveal the cortex. For spine and axon imaging, one to two pieces of custom coverglass (3mm diameter, 0.7mm thickness, Warner Instruments) were adhered to a larger coverglass (8mm diameter, #1.5 thickness, Electron Microscopy Sciences) using optical adhesive (# 71, Norland Products) and placed onto the brain to gently compress the underlying cortex and dampen biological motion during imaging. For population imaging, a single coverglass (5mm diameter, #1.5 thickness, Electron Microscopy Sciences) was adhered to the bottom of a titanium insert and then placed onto the brain. In both cases, a stainless steel retaining ring (5/16-inch internal retaining ring, McMaster-Carr) maintained downward pressure on the cranial window throughout the experiment.

For whole cell recording and optogenetic experiments, the cranial window was filled with agarose (1.6%w/v, Type IIIa, Sigma) and a coverglass placed on top of the agarose. For

pipette access, we drilled holes offset from the center of the coverglass to allow our pipette to approach the center of the cranial window at an oblique angle. The cranial window was hermetically sealed using a stainless steel retaining ring (5/16-inch internal retaining ring, McMaster-Carr), Kwik-Cast (World Precision Instruments), and Vetbond (3M). A 1:1 mixture of 1% tropicamide ophthalmic solution (Akorn) and 10% phenylephrine hydrochloride ophthalmic solution (Akorn) was applied to both eyes to dilate the pupils and retract the nictating membranes. Contact lenses were inserted to protect the eyes. Upon completion of the surgical procedure, isoflurane was gradually reduced (0.6 to 1.5%) and then vecuronium (2 mg kg^{-1} hr^{-1}) or pancuronium (2 mg kg^{-1} hr^{-1}) was delivered IV to immobilize the animal.

Visual stimuli

Visual stimuli were generated using Psychopy[35]. The monitor was typically placed 25 cm from the animal. After mapping somatic direction tuning using a grating protocol, we presented the somatic preferred and null directions of motion while imaging dendrites and dendritic spines. For whole cell recording, we optimized the preferred spatial frequency of the stimulus for the cell being recorded. Typical preferred spatial frequencies ranged from 0.04 to 0.25 cycles per degree.

Two photon imaging

Two photon imaging was performed on a Bergamo II microscope (Thorlabs) running Scanimage[36] 2015 or 2016 (Vidrio Technologies) with 940nm dispersion-compensated excitation provided by an Insight DS+ (Spectraphysics). For spine and axon imaging, power after the objective was limited to <60 mW, dependent on depth. Cells were selected for imaging on the basis of their position relative to large blood vessels, responsiveness to visual stimulation, and lack of prolonged calcium transients resulting from overexpression of GCaMP6s. Images were collected at 30 Hz using bidirectional scanning with 512×512 pixel resolution. Images of somata ranged from 50 to 100 μm on a side, while images of dendrites were ~ 40μm on a side. Images of axons were collected at 512×512 pixel resolution with fields of view ~100μm on a side.

Whole-cell patch-clamp recordings

Recordings were performed by inserting a pipette through an agarose-filled craniotomy, or by using a coverglass with a hole drilled for pipette access. A silver- silver chloride reference electrode was inserted into the agarose or muscle. Recordings were made in current clamp mode.

For measurements of membrane potential tuning, spike tuning, effects of optogenetic inhibition, and connectivity mapping, pipettes of 5–8 MΩ resistance were pulled using borosilicate glass (King Glass) and filled with an intracellular solution containing (in mM) 135 K gluconate, 4 KCl, 10 HEPES, 10 Na_2-phosphocreatine, 4 Mg-ATP, 0.3 Na_3GTP, 0–0.1 Alexa 594 or 488, pH 7.2, 295 mOsm. Neurons were recorded from layer 2/3 (100 to 800 μm below the pia) using a Multiclamp 700B (Molecular Devices). Series resistance and pipette capacitance were corrected online. Series resistance for recordings typically ranged from 20 to 80 MΩ. Analog signals were digitized using Spike2 (CED). For optogenetic

inactivation experiments, a fiber (1mm, NA .63) coupled to a 455nm LED light source (Prizmatix) was lowered to 3–5 mm above the cortical surface. Power density at the cortical surface ranged from 1 to 4 mW/mm^2. Optogenetic stimulation either coincided with visual stimulation, or began with a brief ramp (100 to 300 ms) prior to visual stimulation.

For measurements of synaptic conductances, the internal solution contained (in mM) 135 Cs-MeSO$_4$, 10 QX-314, 4 TEA-Cl, 2 EGTA, 2 MgATP, 10 HEPES, 10 Na$_2$-Phosphocreatine, pH 7.3, 295 mOsm and pipettes were typically 6–9 MΩ. Capacitance compensation was corrected online and series resistance was corrected online or offline. Conductance measurements typically began around 30 minutes after break-in to allow the internal solution of the pipette to dialyze the cell, eliminating action potentials and depolarizing the resting membrane potential as expected with the use of Cs+ and QX-314.

Somatically-targeted optogenetic membrane potential mapping (STOMPM) of connectivity

Connectivity mapping was performed on a custom-built microscope based off previously published designs[30]. A DLP projector (X600, Optoma) with its color wheel removed was mounted to a tilt platform (Siskiyou) and linear stage (Thorlabs). A 50mm f/1.4 SLR lens (Nikkor) was mounted as close as possible to the projector and coupled to an achromatic doublet (AC508–150-A). Light passed through a blue dichroic filter (52–532, Edmund Optics) and was reflected onto the sample using a dichroic mirror (T495LPXR, Chroma), and focused onto the sample using a 35mm f/2.0 SLR lens (Nikkor). Emission light passed through a 105mm f2.0 lens (Nikkor) and an emission filter (FF01–600) and was imaged onto a camera (Xyla, Andor) controlled by Micromanager (http://www.micro-manager.org). Single pixels on the DMD corresponded to ~4 μm at the sample. Diffuse background light was < 0.1 mW/mm^2. Opsin was restricted to the soma using the Kv2.1 targeting motif.[37,38] Before obtaining whole-cell recordings, we focused excitation light on the cortical surface. Upon break-in, we first measured the direction tuning of the cell using a grating protocol. Then, we centered a stimulation grid on the pipette and delivered 25–50 trials of random grid stimulation. Spots were typically 100–200 μm FWHM, 1–3 mW power, and displayed for 100ms. We used positive current injection to depolarize the cell and increase the driving force for IPSPs (reversal potential ~75–70 mV, see Extended Data Fig. 9). We likely underestimate input field sizes due to limitations in the spatial spread of virus injection, blue light absorption in blood vessels, and experimental geometry in which the large patch pipette interferes with light stimulation.

Intrinsic signal imaging

Intrinsic signal imaging was performed on the STOMPM microscope or on the Thorlabs Bergamo II. The cortex was illuminated with blue light to obtain a blood vessel map, after which collimated 630 nm light from an LED (Thorlabs) was directed onto the surface of the brain to measure intrinsic hemodynamic responses. Visually evoked responses were collected at ~50 Hz using an Andor Xyla camera. Visual stimuli were blockwise grating stimuli (8s on, 8s off, .06-.1 cycles per degree, 16 directions).

Fixation and immunostaining

Upon completion of imaging, isoflurane was raised to 5% and 0.5 ml Euthasol given IV. The animal was transcardially perfused with 100 ml of 0.9% NaCl (w/v) and then 500 ml of 4% paraformaldehyde in 0.1 M phosphate buffer (PB). The brain was dissected and post-fixed overnight in 4% PFA in 0.1M PB at 4°C. Cryoprotection was carried out in 30% sucrose for 2 days, at which time tissue was sliced at 50 um on a Leica SM 2010R. Cryosections were rinsed in 0.1M phosphate buffered saline (PBS), blocked in blocking solution containing 1% BSA, 2% normal goat serum, and 0.3% triton X-100 in PBS for 1 hour, and then incubated in mouse anti FlagM2 at 1:500 (sigma cat# F1804) overnight at room temperature. After three washes in buffer, 10 minutes each, the sections were incubated in Alexa goat anti mouse 488 at 1:500 (ThermoFisher, cat # A32723) for 2 hours at room temperature. After incubation, sections were washed two times in 0.1M PBS for 10 minutes each, followed by one wash in 0.1M PB. Sections were then mounted on Superfrost Plus slides (VWR, West Chester, PA) and cover-slipped with Slowfade Gold (ThermoFisher cat# S36936). Control slides were treated without the primary antibody. These control sections showed no labeling. To test the specificity of secondary antibodies, the secondary antibody was applied to the tissue without a primary antibody; no staining was observed in these controls.

Analysis

Calcium imaging—Imaging data were excluded from analysis if motion along the z-axis was detected. Dendrite images were corrected for in-plane motion via a 2D cross-correlation based approach in MATLAB. Axon images were corrected for in-plane motion using a piecewise non-rigid motion correction algorithm[39]. ROIs were drawn in ImageJ; dendritic ROIs spanned contiguous dendritic segments and bouton/spine ROIs were circular. Mean pixel values for single ROIs were computed over the imaging time series and imported into MATLAB via MIJ[40]. $\Delta F/F_0$ was computed by defining F_0 using a 60s percentile filter (typically 10^{th} percentile), which was then low pass filtered at 0.01 Hz. Bouton and somatic responses were computed as the average response to the visual stimulus and were included for analysis of direction selectivity if $\Delta F/F_0$ exceeded 10% and 1-CV was > 0.1. $\Delta F/F_0$ traces were median filtered with a 3 sample window. For spine signals, we subtracted a scaled version of the dendritic signal to remove backpropagating action potentials as performed previously[12,13]. $\Delta F/F_0$ traces were synchronized to stimulus triggers sent from Psychopy and collected by Spike2. Spines were included for analysis if the average response exceeded 2 median absolute deviations above the baseline noise (measured during the blank) and were weakly correlated with the dendritic signal (Spearman's correlation, $r<0.3$). Some spine traces contained negative events after subtraction, so we set negative ΔF/F values to NaN's when computing Spearman's correlation between the spine and the dendrite. Because the amplitude of NMDA receptor mediated calcium transients are not necessarily correlated with EPSP amplitude at the soma[41], we normalized each spine's responses so that each spine had equal weight when computing summed spine inputs. Summed spine inputs were computed as the average spine response to each stimulus, bootstrapped 100 times. We also compared tuning of populations of spine inputs to somatic output by including response amplitude in the calculation and by computing the fraction of spines that preferentially respond to the preferred direction.

Direction selectivity index (DSI) was computed as:

$$\frac{Preferred - Null}{Preferred + Null}$$

Whole-cell recording—Membrane potential recordings were median filtered with a 30 to 100 sample window to remove action potentials and binned to 5 ms. Responses to individual stimulus cycles were extracted for V_m and spikes separately. Mean (F0) and modulation amplitudes (F1 and F2) of each cycle were computed via Fast Fourier Transform (Matlab). V_m and spiking peak responses were computed as described previously[14]. Some cells exhibited V_m modulation at F2, so we also included the F2 component when computing V_m responses. For computing V_m noise, we aligned cycle responses across trials, then took the standard deviation for each timepoint. V_m standard deviation was computed as the mean of this standard deviation value for each stimulus.

Conductance measurements were made in current-clamp mode[11,14]. Multiple current steps depolarized or hyperpolarized the neuron close to the reversal potential for inhibition and excitation, respectively. Leak-subtracted synaptic conductances were computed by estimating G_{leak} using the blank stimulus and then performing a linear fit of measured membrane potential responses at different current injections. Mean and standard deviation of synaptic conductances were computed with a bootstrap (100 iterations). Cells were excluded from further analysis if negative conductances were extracted across multiple stimuli. To predict membrane potential responses from empirically measured synaptic conductances, we computed stimulus-dependent responses as described previously[22]:

$$\Delta V(\theta) = \frac{g_L R_L + g_e(\theta) R_e + g_i(\theta) R_i}{g_L + g_e(\theta) + g_i(\theta)} - V_r$$

Where R_L is −50 mV, V_r is −50 mV, R_e is 0 mV, R_i is −70 mV, θ is the direction of motion. g_L is the measured leak conductance, and $g_e(\theta)$ and $g_i(\theta)$ are measured synaptic conductances.

Optogenetic stimulation experiments compared visually evoked subthreshold responses under blue light stimulation with the responses obtained without blue light stimulation. Modulation ratio was computed as the response amplitude with blue light on divided by the response amplitude with blue light off.

For connectivity mapping, membrane potential traces were median filtered with a time window of 1.2 ms. We defined the prestimulus membrane potential as the membrane potential in the 9 ms before IPSP onset. Because of spontaneous activity *in vivo*, single trials were excluded if cells showed large depolarizations (>5 mV) relative to the prestimulus membrane potential. Significant IPSPs were defined as average IPSPs exceeding three standard deviations below the mean of the prestimulus membrane potential. We used the centroid of the significant IPSP field for distance measurements from single cells. Ellipse

fits of the binarized significant IPSP array were computed using the MATLAB function 'regionprops.m'.

Intrinsic signal imaging—Single-condition maps were computed by comparing whether reflectance changes evoked by a single-stimulus condition could be discriminated from reflectance changes evoked across all presented stimuli[42]. To discriminate a single-condition stimulus at each pixel, reflectance changes across all stimuli were combined into a normalized histogram, and then a pixel's single condition response was computed non-parametrically as the probability of the area under a ROC curve (using the trapezoidal rule). Maps were filtered as previously described using a bandpass fermi filter[12]. Single bouton direction preferences were compared to the direction preference of the intrinsic signal direction preference map contained within the 100 μm two photon field of view. Somatic direction preference was compared to the direction preference of the intrinsic map at the location of the cell. For STOMPM, stimulation grids were aligned to blood vessel reference maps for intrinsic signal imaging using an affine transform. We computed binary masks for each stimulation spot, and used these masks to measure intrinsic signal direction preference at single stimulation spots.

Statistics—Sample sizes are similar to others used in the field. Sample size was not determined prior to experiments. Inclusion criteria for each experiment are detailed for methods. No randomization was utilized. The experimenter was blind to location in the direction preference map when performing map-related experiments. To test whether two distributions of direction preference were significantly different from random, we compared the median difference with a null distribution generated from Monte Carlo simulations (n=1,000). For each Monte Carlo simulation, we calculated the median difference between two randomly sampled distributions of direction preferences drawn from a uniform distribution ranging from 0° to 359° with sample sizes equivalent to the measured distributions. Statistical tests were non-parametric and two-sided, except for the Monte Carlo significance tests, which were one-sided.

All correlations values reported were computed using Spearman's correlation.

Code availability—Analyses were performed using MATLAB using standard functions. Custom code is available from the corresponding author upon reasonable request.

Data availability—Source data are provided for graphical data representations in Figs. 1d,e,f, 2c,d,e,f,g, 3c,d,e,f,h,i,j, and 4f,k,m,n. Data are available from the corresponding author upon reasonable request.

Extended Data

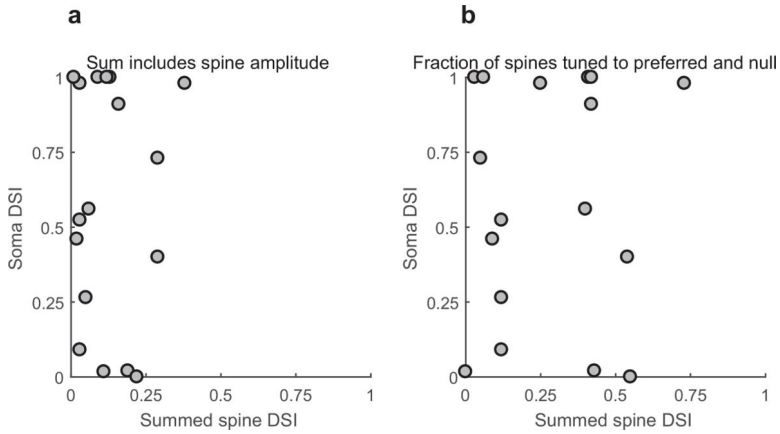

Extended Data 1: Summed spine inputs fail to predict somatic direction selectivity, regardless of the method used to compute the sum

a, No significant correlation between the DSI of summed spine inputs (with amplitude included) and somatic DSI. Spearman's $r = -.11$, $P = .68$, $n = 17$. **b**, No significant correlation between the fraction of spines that respond more strongly to the preferred direction and somatic DSI. Spearman's $r = -.082$, $P = .75$, $n = 17$.

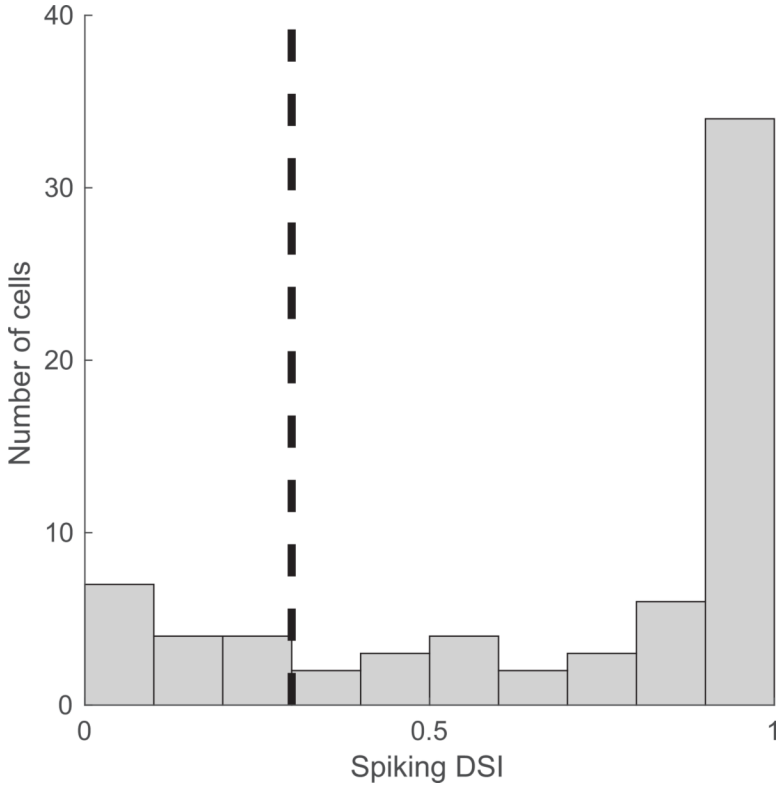

Extended Data Figure 2: Distribution of spiking DSI

Dashed line indicates cutoff of DSI>.3; $n = 69$ cells with spiking responses.

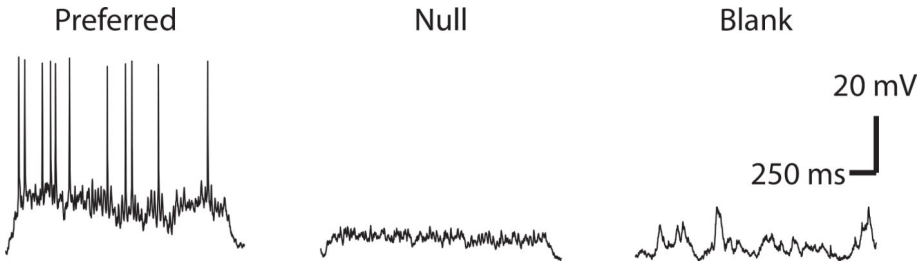

Extended Data Figure 3: Example of noise suppression at null stimulus relative to blank

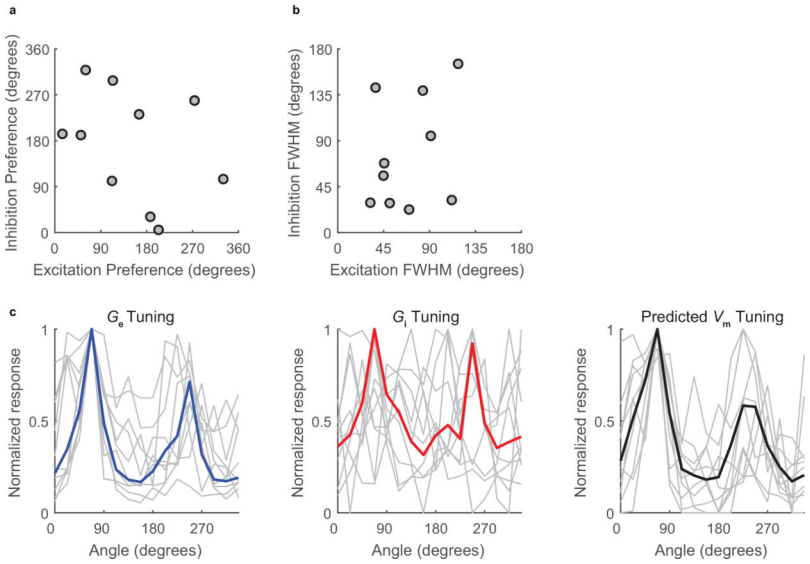

Extended Data Figure 4: Direction tuning fits for excitatory and inhibitory conductances

a, Difference in direction preference of excitation and inhibition are significantly greater than chance; Monte Carlo significance test, p=.023; difference in direction preference, 135±95 degrees, median ± IQR, n = 10 cells from 7 animals. **b**, FWHM (full width half-max) of excitation and inhibition were not significantly different. FWHM 61±46 and 61±110 degrees for excitation and inhibition, respectively, median ± IQR, n=10, Wilcoxon Sign-Rank (WSR) P = .70. **c**, individual (grey) and population average (colored) tuning curves for G_e, G_i, and predicted V_m, peak-aligned to excitation

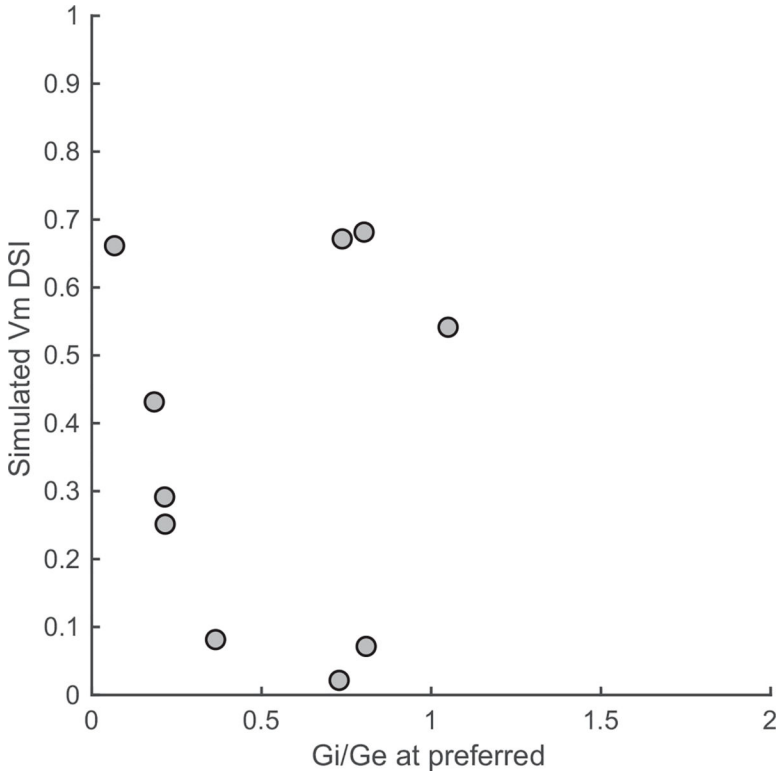

Extended Data Figure 5: I/E ratio at preferred direction is not correlated with simulated subthreshold direction selectivity

Spearman's $r = .0061$, $P = 1$, $n = 10$ cells from 7 animals

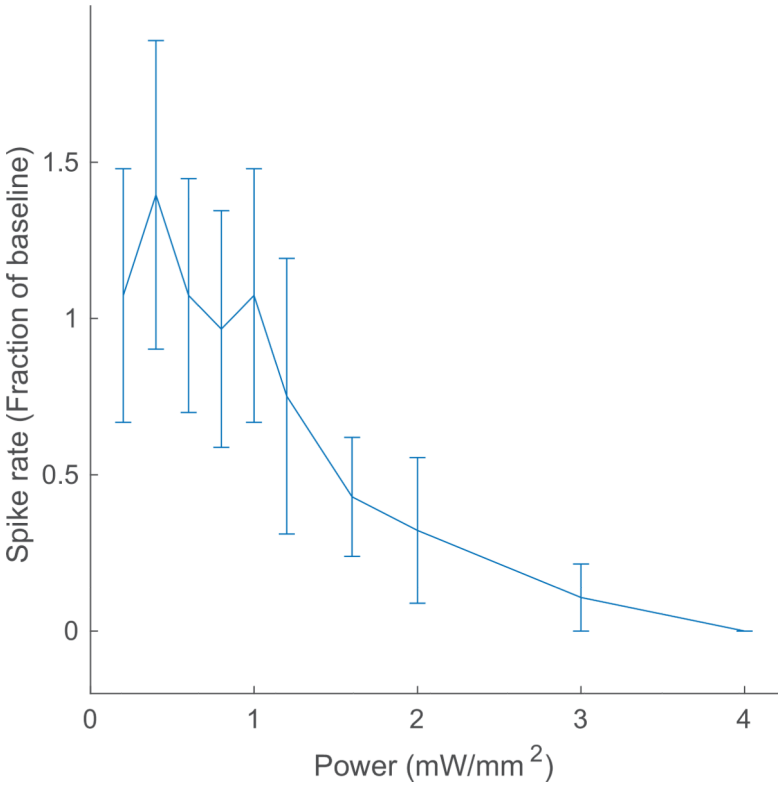

Extended Data Figure 6: Putative GABAergic neuron directly suppressed by blue light
Error bars are mean ± SEM

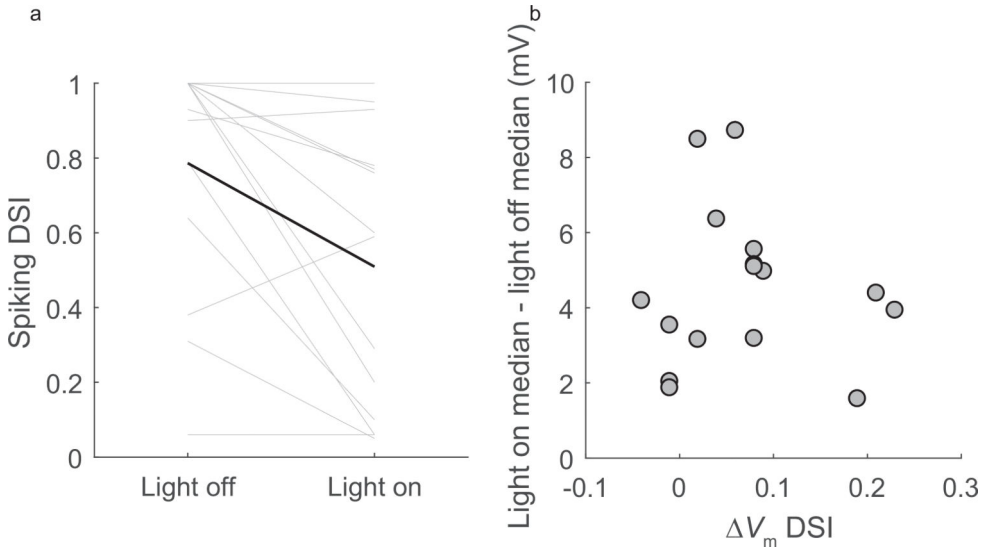

Extended Data Figure 7: Additional data related to blue light photoinhibition of GABAergic neurons

a, Optogenetically suppressing GABAergic neurons significantly reduces spiking direction selectivity; WSR, $n = 14$ cells with spiking responses, $P = .0049$. Black line is mean and grey lines are single cells. **b**, absolute V_m depolarization induced by blue light is not related to optogenetic changes in V_m direction selectivity (computed as the difference in DSI between light off and light on conditions); Spearman's $r = .11$, $P = .70$, $n = 14$ cells with spiking responses from 4 animals

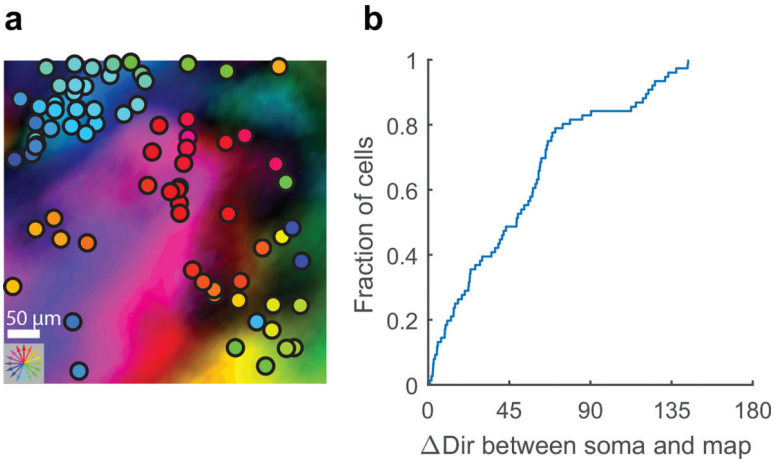

Extended Data Figure 8: Alignment of GABAergic neurons with intrinsic signal polar direction map

a, Underlying intrinsic signal polar direction map with direction-tuned GABAergic neurons overlaid. **b**, Direction preferences of inhibitory neurons and intrinsic signal direction preference map are significantly more similar than chance; p<.001, Monte Carlo significance test, $n = 76$ direction-selective neurons from 3 planes in 1 animal.

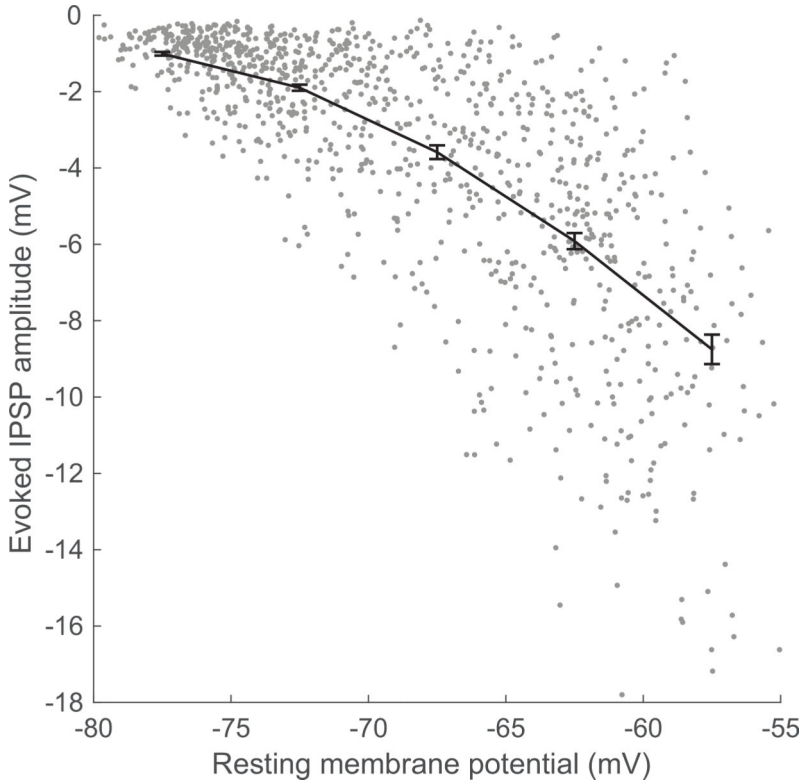

Extended Data Figure 9: Reversal potential of optogenetically evoked PSPs is consistent with inhibition

Grey points are individual data points; black is mean ± SEM. Data come from individual stimulation trials from one cell.

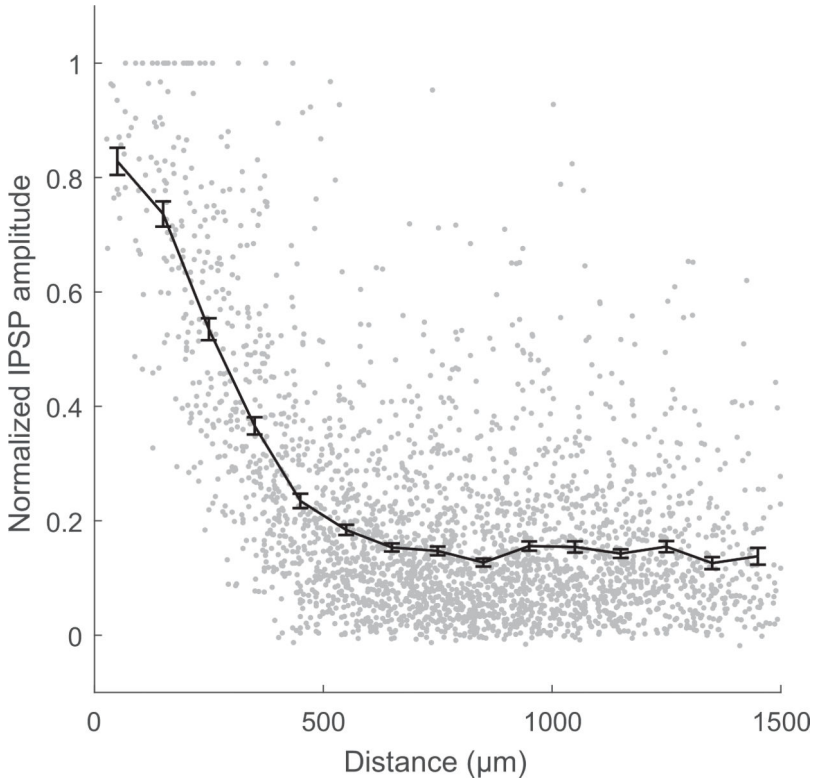

Extended Data Figure 10: Relationship of IPSP amplitude versus distance

Grey points are individual data points; black is binned mean ± SEM. Data come from trial-averaged stimulation responses from $n = 21$ cells from 7 animals

Supplementary Material

Refer to Web version on PubMed Central for supplementary material.

Acknowledgements

The authors thank David Whitney for help with analysis, Arkarup Banerjee and Florin Albeanu for help with patterned photostimulation setup, Jeremy Chang for discussions about optogenetic stimulation, Dominique Ouimet for surgical assistance, Nicole Shultz and Rachel Satterfield for histology, Tal Laviv for discussions about CyRFP, and Chris Baker and McLean Bolton for cloning and the gift of the ChR2 construct. The authors thank the GENIE project for access to GCaMP6. This work was supported by EY011488, the Max Planck Florida Institute for Neuroscience, and the Max Planck Society.

Main References

1. Cossell L et al. Functional organization of excitatory synaptic strength in primary visual cortex. Nature 518, 399–403, doi:10.1038/nature14182 (2015). [PubMed: 25652823]
2. Ko H et al. Functional specificity of local synaptic connections in neocortical networks. Nature 473, 87–91, doi:10.1038/nature09880 (2011). [PubMed: 21478872]
3. Lee WC et al. Anatomy and function of an excitatory network in the visual cortex. Nature 532, 370–374, doi:10.1038/nature17192 (2016). [PubMed: 27018655]
4. Tan AY, Brown BD, Scholl B, Mohanty D & Priebe NJ Orientation selectivity of synaptic input to neurons in mouse and cat primary visual cortex. The Journal of neuroscience : the official journal of

the Society for Neuroscience 31, 12339–12350, doi:10.1523/JNEUROSCI.2039-11.2011 (2011). [PubMed: 21865476]

5. Monier C, Chavane F, Baudot P, Graham LJ & Fregnac Y Orientation and direction selectivity of synaptic inputs in visual cortical neurons: a diversity of combinations produces spike tuning. Neuron 37, 663–680 (2003). [PubMed: 12597863]
6. Liu BH et al. Broad inhibition sharpens orientation selectivity by expanding input dynamic range in mouse simple cells. Neuron 71, 542–554, doi:10.1016/j.neuron.2011.06.017 (2011). [PubMed: 21835349]
7. Smith SL, Smith IT, Branco T & Hausser M Dendritic spikes enhance stimulus selectivity in cortical neurons in vivo. Nature 503, 115–120, doi:10.1038/nature12600 (2013). [PubMed: 24162850]
8. Palmer LM et al. NMDA spikes enhance action potential generation during sensory input. Nature neuroscience 17, 383–390, doi:10.1038/nn.3646 (2014). [PubMed: 24487231]
9. Lavzin M, Rapoport S, Polsky A, Garion L & Schiller J Nonlinear dendritic processing determines angular tuning of barrel cortex neurons in vivo. Nature 490, 397–401, doi:10.1038/nature11451 (2012). [PubMed: 22940864]
10. Priebe NJ & Ferster D Inhibition, spike threshold, and stimulus selectivity in primary visual cortex. Neuron 57, 482–497, doi:10.1016/j.neuron.2008.02.005 (2008). [PubMed: 18304479]
11. Anderson JS, Carandini M & Ferster D Orientation tuning of input conductance, excitation, and inhibition in cat primary visual cortex. Journal of neurophysiology 84, 909–926 (2000). [PubMed: 10938316]
12. Wilson DE, Whitney DE, Scholl B & Fitzpatrick D Orientation selectivity and the functional clustering of synaptic inputs in primary visual cortex. Nature neuroscience 19, 1003–1009, doi: 10.1038/nn.4323 (2016). [PubMed: 27294510]
13. Chen TW et al. Ultrasensitive fluorescent proteins for imaging neuronal activity. Nature 499, 295–300, doi:10.1038/nature12354 (2013). [PubMed: 23868258]
14. Priebe NJ & Ferster D Direction selectivity of excitation and inhibition in simple cells of the cat primary visual cortex. Neuron 45, 133–145, doi:10.1016/j.neuron.2004.12.024 (2005). [PubMed: 15629708]
15. Torre V & Poggio T A Synaptic Mechanism Possibly Underlying Directional Selectivity to Motion. Proceedings of the Royal Society B: Biological Sciences 202, 409–416, doi:10.1098/rspb. 1978.0075 (1978).
16. Sillito AM Inhibitory processes underlying the directional specificity of simple, complex and hypercomplex cells in the cat's visual cortex. The Journal of physiology 271, 699–720 (1977). [PubMed: 926020]
17. Prescott SA & De Koninck Y Gain control of firing rate by shunting inhibition: roles of synaptic noise and dendritic saturation. Proceedings of the National Academy of Sciences of the United States of America 100, 2076–2081, doi:10.1073/pnas.0337591100 (2003). [PubMed: 12569169]
18. Chance FS, Abbott LF & Reyes AD Gain modulation from background synaptic input. Neuron 35, 773–782 (2002). [PubMed: 12194875]
19. Katzner S, Busse L & Carandini M GABAA inhibition controls response gain in visual cortex. The Journal of neuroscience : the official journal of the Society for Neuroscience 31, 5931–5941, doi: 10.1523/JNEUROSCI.5753-10.2011 (2011). [PubMed: 21508218]
20. Isaacson JS & Scanziani M How inhibition shapes cortical activity. Neuron 72, 231–243, doi: 10.1016/j.neuron.2011.09.027 (2011). [PubMed: 22017986]
21. Wehr M & Zador AM Balanced inhibition underlies tuning and sharpens spike timing in auditory cortex. Nature 426, 442–446, doi:10.1038/nature02116 (2003). [PubMed: 14647382]
22. Atallah BV, Bruns W, Carandini M & Scanziani M Parvalbumin-expressing interneurons linearly transform cortical responses to visual stimuli. Neuron 73, 159–170, doi:10.1016/j.neuron. 2011.12.013 (2012). [PubMed: 22243754]
23. Crook JM, Kisvarday ZF & Eysel UT Evidence for a contribution of lateral inhibition to orientation tuning and direction selectivity in cat visual cortex: reversible inactivation of functionally characterized sites combined with neuroanatomical tracing techniques. The European journal of neuroscience 10, 2056–2075 (1998). [PubMed: 9753093]

24. Wilson DE et al. GABAergic Neurons in Ferret Visual Cortex Participate in Functionally Specific Networks. Neuron 93, 1058–1065 e1054, doi:10.1016/j.neuron.2017.02.035 (2017). [PubMed: 28279352]

25. Packer AM & Yuste R Dense, unspecific connectivity of neocortical parvalbumin-positive interneurons: a canonical microcircuit for inhibition? The Journal of neuroscience : the official journal of the Society for Neuroscience 31, 13260–13271, doi:10.1523/JNEUROSCI.3131-11.2011 (2011). [PubMed: 21917809]

26. Hofer SB et al. Differential connectivity and response dynamics of excitatory and inhibitory neurons in visual cortex. Nature neuroscience 14, 1045–1052, doi:10.1038/nn.2876 (2011). [PubMed: 21765421]

27. Levy RB & Reyes AD Spatial profile of excitatory and inhibitory synaptic connectivity in mouse primary auditory cortex. The Journal of neuroscience : the official journal of the Society for Neuroscience 32, 5609–5619, doi:10.1523/JNEUROSCI.5158-11.2012 (2012). [PubMed: 22514322]

28. Martin KA, Somogyi P & Whitteridge D Physiological and morphological properties of identified basket cells in the cat's visual cortex. Experimental brain research 50, 193–200 (1983). [PubMed: 6641854]

29. Roerig B & Chen B Relationships of local inhibitory and excitatory circuits to orientation preference maps in ferret visual cortex. Cereb Cortex 12, 187–198 (2002). [PubMed: 11739266]

30. Dhawale AK, Hagiwara A, Bhalla US, Murthy VN & Albeanu DF Non-redundant odor coding by sister mitral cells revealed by light addressable glomeruli in the mouse. Nature neuroscience 13, 1404–1412, doi:10.1038/nn.2673 (2010). [PubMed: 20953197]

31. Li YT, Liu BH, Chou XL, Zhang LI & Tao HW Strengthening of Direction Selectivity by Broadly Tuned and Spatiotemporally Slightly Offset Inhibition in Mouse Visual Cortex. Cereb Cortex 25, 2466–2477, doi:10.1093/cercor/bhu049 (2015). [PubMed: 24654259]

32. Borst A & Helmstaedter M Common circuit design in fly and mammalian motion vision. Nature neuroscience 18, 1067–1076, doi:10.1038/nn.4050 (2015). [PubMed: 26120965]

Methods References

33. Dimidschstein J et al. A viral strategy for targeting and manipulating interneurons across vertebrate species. Nature neuroscience 19, 1743–1749, doi:10.1038/nn.4430 (2016). [PubMed: 27798629]

34. Govorunova EG, Sineshchekov OA, Janz R, Liu X & Spudich JL NEUROSCIENCE. Natural light-gated anion channels: A family of microbial rhodopsins for advanced optogenetics. Science 349, 647–650, doi:10.1126/science.aaa7484 (2015). [PubMed: 26113638]

35. Peirce JW PsychoPy--Psychophysics software in Python. Journal of neuroscience methods 162, 8–13, doi:10.1016/j.jneumeth.2006.11.017 (2007). [PubMed: 17254636]

36. Pologruto TA, Sabatini BL & Svoboda K ScanImage: flexible software for operating laser scanning microscopes. Biomedical engineering online 2, 13, doi:10.1186/1475-925X-2-13 (2003). [PubMed: 12801419]

37. Baker CA, Elyada YM, Parra A & Bolton MM Cellular resolution circuit mapping with temporal-focused excitation of soma-targeted channelrhodopsin. eLife 5, doi:10.7554/eLife.14193 (2016).

38. Wu C, Ivanova E, Zhang Y & Pan ZH rAAV-mediated subcellular targeting of optogenetic tools in retinal ganglion cells in vivo. PloS one 8, e66332, doi:10.1371/journal.pone.0066332 (2013). [PubMed: 23799092]

39. Pnevmatikakis EA & Giovannucci A NoRMCorre: An online algorithm for piecewise rigid motion correction of calcium imaging data. Journal of neuroscience methods 291, 83–94, doi:10.1016/j.jneumeth.2017.07.031 (2017). [PubMed: 28782629]

40. Sage D, Prodanov D, Tinevez JY, Schindelin J in ImageJ User & Developer Conference (Luxembourg, 2012).

41. Sobczyk A, Scheuss V & Svoboda K NMDA receptor subunit-dependent [Ca2+] signaling in individual hippocampal dendritic spines. The Journal of neuroscience : the official journal of the Society for Neuroscience 25, 6037–6046, doi:10.1523/JNEUROSCI.1221-05.2005 (2005). [PubMed: 15987933]

42. Purushothaman G, Khaytin I & Casagrande VA Quantification of optical images of cortical responses for inferring functional maps. Journal of neurophysiology 101, 2708–2724, doi: 10.1152/jn.90696.2008 (2009). [PubMed: 19225176]

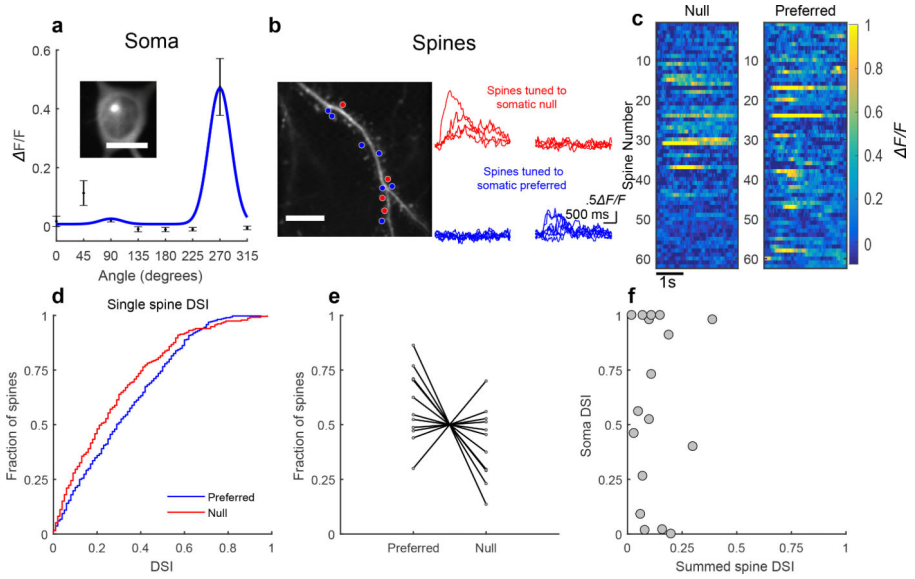

Figure 1: Direction tuning of excitatory synaptic inputs onto layer 2/3 neurons in ferret V1

a, Example soma tuning; data are mean ± s.e.m.; scale bar is 10 μm. **b,** (left) Example dendritic spines (n = 11) pseudocolored for direction preference; scale bar is 10 μm; (right) Spine trial averaged responses to somatic preferred or null directions. **c,** Trial averaged responses for all significantly responsive spines (n = 62) from cell in **a**. **d**, DSI distributions for preferred (n = 384) and null (n = 233) directions tuned spines. **e,** Fraction of spines on direction-selective cells (n = 12) preferring somatic preferred and null directions. **f**, Relationship between somatic DSI and summed spine DSI (n = 17 cells from 10 animals).

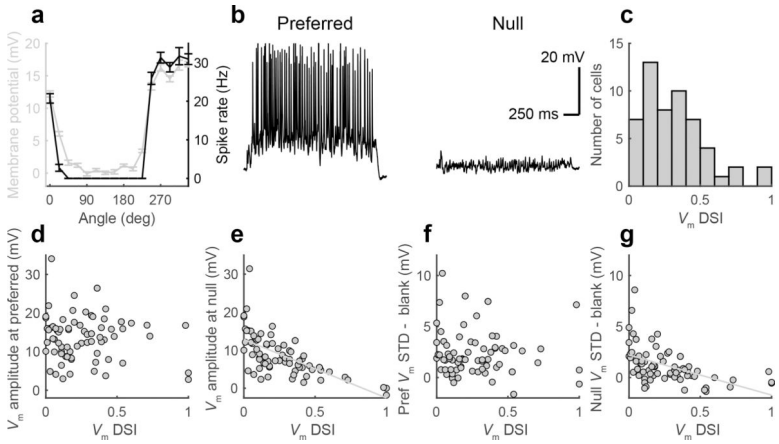

Figure 2: Subthreshold direction selectivity and evidence for null direction suppression

a, Example direction tuning of subthreshold V_m (grey) and spiking responses (black). **b**, Example single trial responses. **c**, Distribution of V_m DSI for 54 cells with direction-selective spiking (DSI > 0.3). **d**, No relationship between preferred direction response and V_m DSI (n = 76 from 23 animals). **e**, Relationship between null direction response and V_m DSI; gray line is least-squares fit (n = 76). **f**, No relationship between preferred direction V_m noise (trial-to-trial variability) and V_m DSI (n = 76). **g**, Relationship between null direction V_m noise and V_m DSI; gray line is least-squares fit (n = 76).

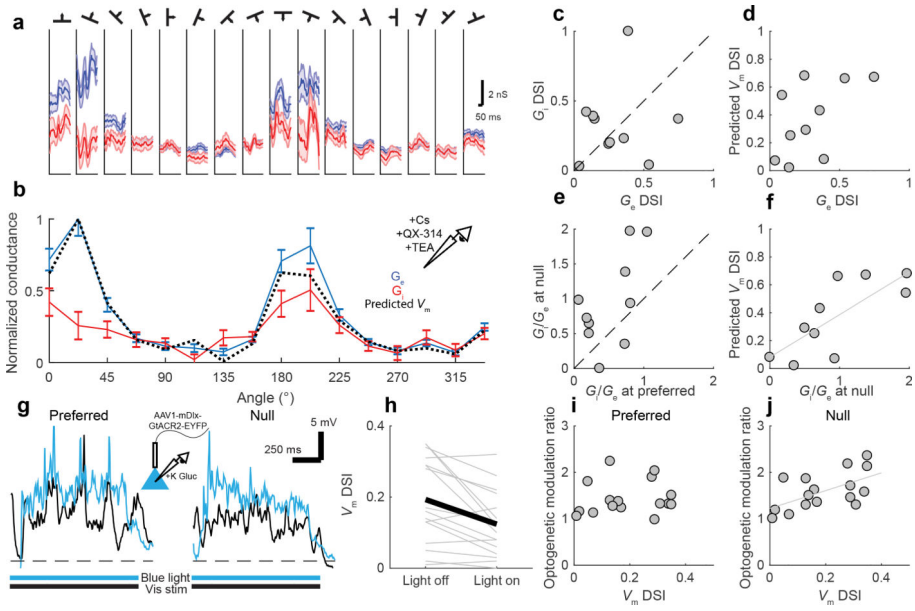

Figure 3: Differential tuning between excitation and inhibition enhances direction selectivity

a, Estimated excitatory (blue, G_e) and inhibitory (red, G_i) synaptic conductances driven by gratings from an example cell; line is bootstrapped mean and error bars are bootstrapped s.d.. **b**, Tuning of peak (see Methods) synaptic conductances and predicted V_m (dashed line) for cell in **a**; data are bootstrapped mean and s.d.. **c**, Comparison of G_e and G_i DSI ($n = 10$ from 7 animals). **d**, Predicted V_m DSI (see Methods) compared to G_e DSI ($n = 10$). **e**, Comparison of G_i/G_e at null and preferred directions ($n = 10$). **f**, Predicted V_m DSI compared to null direction G_i/G_e; gray line is least-squares fit ($n = 10$). **g**, Example V_m during visual stimulation and inactivation of GABAergic neurons expressing GtACR2 (cyan) or without inactivation (black); dashed line is resting V_m. **h**, Comparison of V_m DSI with and without inactivation; black line indicates population means ($n = 16$ from 4 animals). **i**, Optogenetic modulation of preferred direction response versus V_m DSI ($n = 16$). **j**, Optogenetic modulation of null direction response versus V_m DSI; gray line is least-squares fit ($n = 16$).

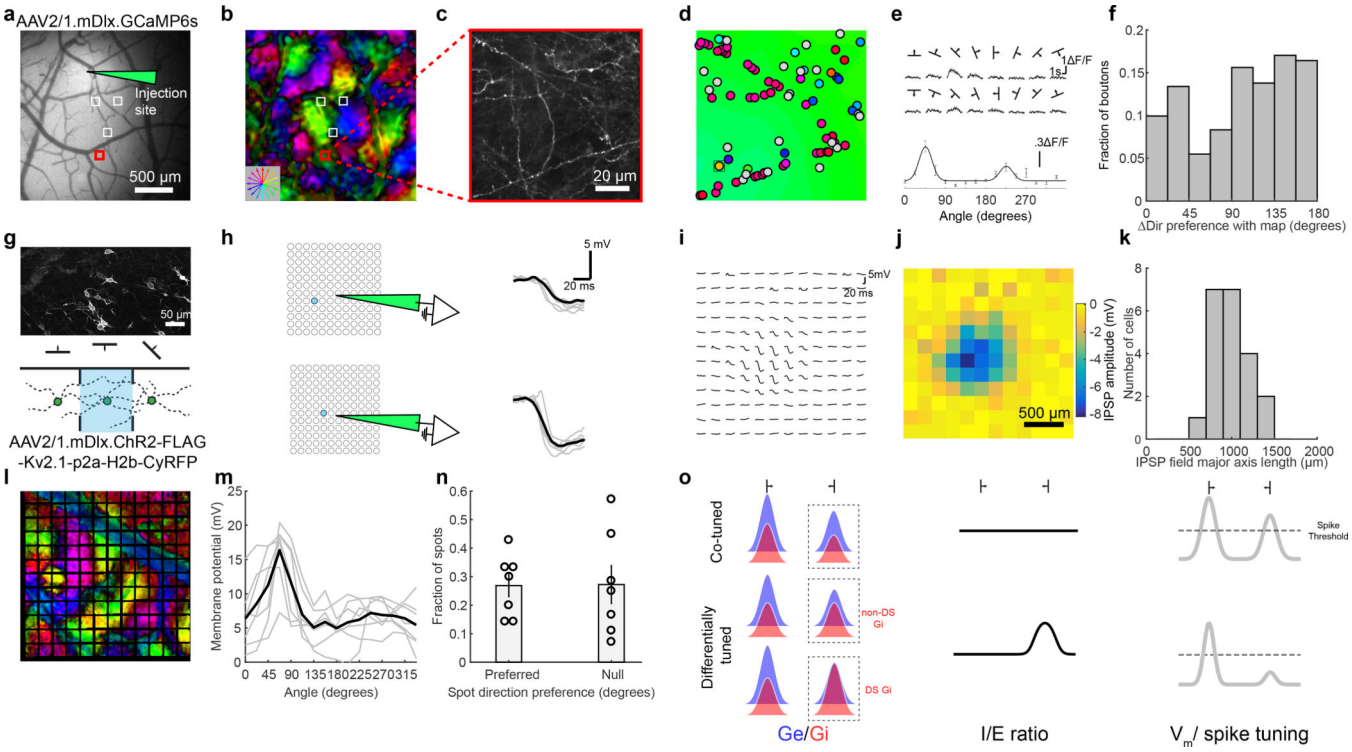

Figure 4: Inhibitory interneurons make long-range, intercolumnar projections onto excitatory neurons

a, Epifluorescence image of injection site with GABAergic-axon imaging sites highlighted; example FOV in red. **b**, Intrinsic signal polar direction map for **a**. **c**, Example bouton FOV. **d**, GABAergic boutons overlaid on direction preference map; direction preference of boutons and intrinsic signal pseudocolored as in b.; bi-directional boutons colored grey. **e**, example bouton tuning curve (box in d); data are mean ± s.e.m.. **f**, Distribution of direction preference difference between GABAergic boutons (n = 493) and corresponding intrinsic signal direction preference map; **g**, *Top*: FLAG staining of cells expressing AAV1-mDlx-ChR2-FLAG-Kv2.1-p2a-H2b-CyRFP; *Bottom*: Experimental design: neurons in different cortical columns are optogenetically activated. **h**, Example of single spot illumination and V_m responses. **i**, Mean IPSP waveforms evoked by sampled spots. **j**, Map of IPSP amplitudes. **k**, Distribution of IPSP-field major axis lengths across cells (n = 21). **l**, Example aligned stimulation grid to intrinsic signal polar direction map. **m**, Peak-aligned average direction tuning curve for cells with direction-tuned membrane potential (DSI > 0.3, black, individual cells in grey, n = 7). **n**, Fraction of spots tuned to a cell's preferred (<45°) or null (>135°) direction (gray bars are mean ± s.e.m.), **o**, Cartoon model of co-tuning (*top*) and differential tuning (*bottom*) of excitation (G_e) and inhibition (G_i) for direction. Subthreshold direction selectivity is inherited from synaptic conductances when co-tuned. Differential tuning of G_e and G_i, whereby there is greater G_i/G_e at the null direction, can preferentially suppress excitation and enhance subthreshold selectivity. With differential tuning, inhibition can either be bidirectional or oppositely tuned for direction relative to G_e.